Journal of Materials Chemistry

www.rsc.org/materials

Volume 17 | Number 30 | 14 August 2007 | Pages 3053–3272

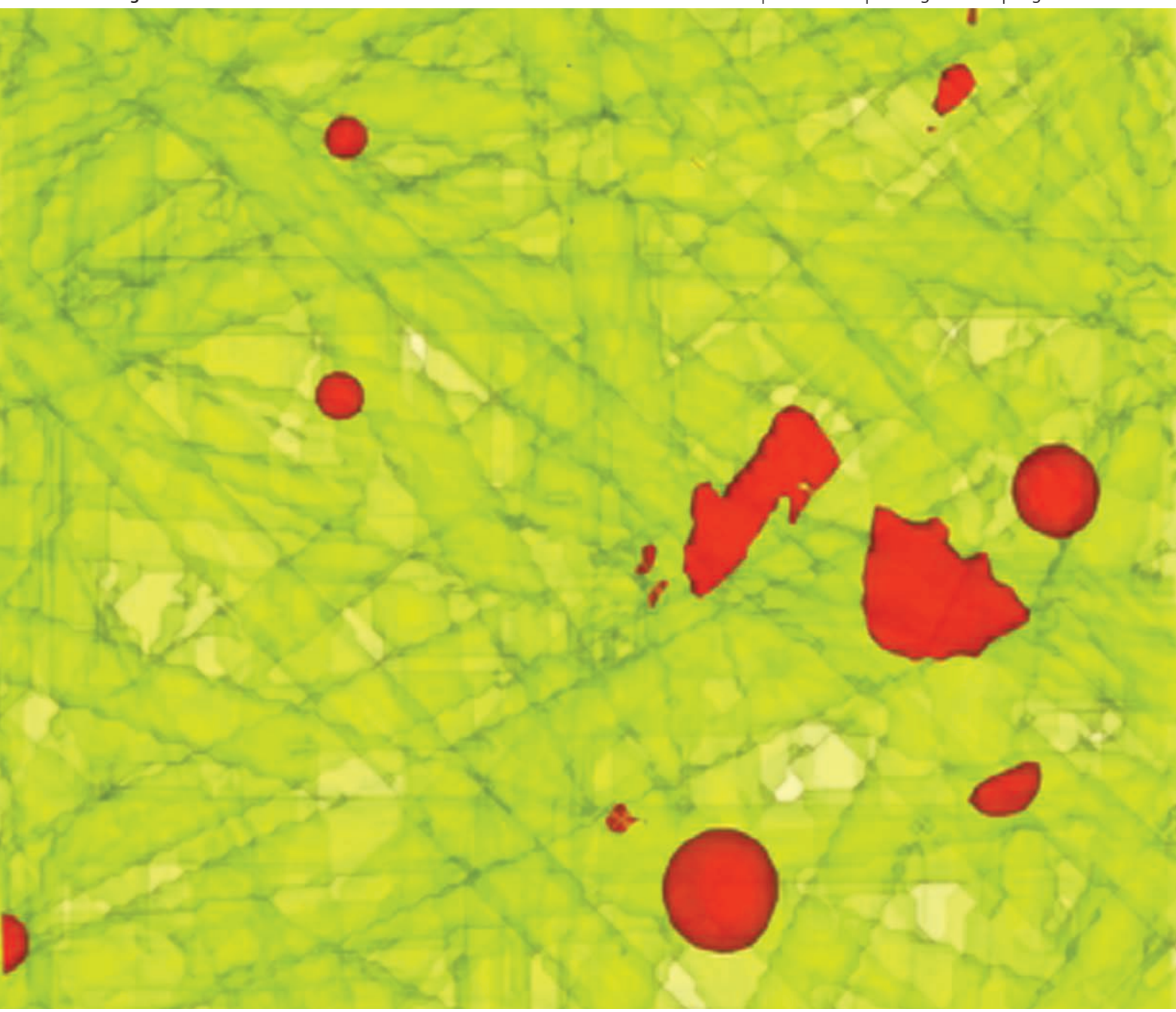

ISSN 0959-9428

Impact of GDL structure and wettability on water management in polymer electrolyte fuel cells†

Puneet K. Sinha,‡ Partha P. Mukherjee‡ and Chao-Yang Wang*

Received 7th March 2007, Accepted 16th April 2007
First published as an Advance Article on the web 8th May 2007
DOI: 10.1039/b703485g

A key performance limitation in polymer electrolyte fuel cells (PEFC), called the mass transport loss, originates from liquid water transport and resulting flooding phenomena in the constituent components. The cathode gas diffusion layer (GDL) is a primary contributor to mass transport loss owing to the blockage of available pore space by liquid water thereby rendering hindered oxygen transport to the active reaction sites in the electrode. The GDL, typically a fibrous non-woven carbon paper or a woven carbon cloth, thus plays an important role in the water management of a PEFC. This Feature Article provides a systematic description of the development of pore-scale models coupled with realistic microstructural delineation as well as micron-resolution imaging techniques to study the profound influence of the underlying structure and surface wettability on liquid water transport and interfacial dynamics in the fuel cell GDL. A pore-network model and a two-phase lattice Boltzmann model coupled with stochastic generation of GDL microstructures are elaborated. Concurrently, optical diagnostics of water dynamics at GDL interfaces and X-ray micro-tomographic imaging of liquid water distribution inside the GDL of an operating fuel cell are discussed.

1. Introduction

Fuel cells, owing to their high energy efficiency, environmental friendliness and minimal noise, are widely considered as the 21st century energy-conversion devices for portable, mobile and stationary power. Among the several types of fuel cells, the polymer electrolyte fuel cell (PEFC) has emerged as the most promising power source for a broad range of applications. Despite tremendous recent progress in overall cell performance, a pivotal performance/durability limitation in PEFCs centers on liquid water transport and resulting flooding in the constituent components. Liquid water blocks the reactant-transporting porous network in the gas diffusion layer (GDL), hindering oxygen transport to the active reaction sites in the catalyst layer (CL) and causing mass transport losses. The GDL, therefore, plays a crucial role in the water management which dictates a delicate balance between membrane hydration and water removal from the CL and GDL.

While considerable research, both modeling and experimental,[1–3] has been conducted to study flooding and water transport in PEFCs, fundamental understanding of liquid

Electrochemical Engine Center (ECEC), and Department of Mechanical and Nuclear Engineering, The Pennsylvania State University, University Park, PA, 16802, USA. E-mail: cxw31@psu.edu
† This paper is part of a *Journal of Materials Chemistry* theme issue on New Energy Materials. Guest editor: M. Saiful Islam.
‡ Equal contributors to this work.

Puneet K. Sinha

Puneet Sinha is a Ph.D. student in Professor Chao-Yang Wang's group in the Department of Mechanical and Nuclear Engineering, Pennsylvania State University. He obtained a M.S. in mechanical engineering at The Pennsylvania State University in 2006 and a B. Tech. in mechanical engineering at the Institute of Technology, Banaras Hindu University, India in 2003. His research interests include fundamental pore-scale modeling and characterization of liquid water transport in fuel cells.

Partha P. Mukherjee

Partha P. Mukherjee is a Ph.D. candidate working with Professor Chao-Yang Wang in the Electrochemical Engine Center (ECEC), Pennsylvania State University (PSU), USA. He holds a B.S. degree (1997) from North Bengal University, India and a M.S. degree (1999) from Indian Institute of Technology, Kanpur, India. He worked as a consulting engineer for four years in Fluent India Pvt. Ltd, a fully owned subsidiary of Ansys–Fluent, USA, prior to joining PSU in 2003. His research interests include transport phenomena in fuel cells and pore-scale physics.

water dynamics in GDL at the pore-level remains largely absent, leading to the following critical questions:

(1) What is the liquid water transport mechanism through a fibrous GDL structure? What is the influence of the structural and wetting characteristics on liquid water removal from the GDL? What should be a basic building block of fuel cell GDL?

(2) What are the mechanisms and influences of liquid water transport and coverage at the GDL surface facing the gas channel?

The current research on GDL flooding is represented by the development of macroscopic models and imaging techniques for liquid water transport in GDL.[4–9] Existing efforts based on neutron radiography (NR) and magnetic resonance imaging (MRI), owing to their low spatial resolution (~25 μm), 2-D nature, and magnetic field sensitivity to carbon, have not been able to yield data of liquid water distribution in a fuel cell GDL.[10] The macroscopic models based on the theory of volume averaging fail to take into account the influence of structural morphology. In order to resolve the open questions regarding liquid water transport through a GDL, a two-pronged approach consisting of micron-resolution imaging and pore-level modeling is warranted. Pore-scale modeling and experimentation are envisioned to unveil the underlying two-phase dynamics as well as to quantify structure–wettability–performance relationship of the GDL, thus leading to novel water management strategies for PEFCs.

This Feature Article presents an account of recent efforts in pore-scale modeling and micron-resolution characterization to address liquid water transport and interfacial dynamics of the GDL in a PEFC.

2. GDL structural and wetting characteristics

The multi-faceted functionality of a GDL includes reactant distribution, liquid water transport, electron transport, heat conduction and mechanical support to the membrane-electrode assembly. For the purpose of liquid water removal, a GDL can be characterized by two independent parameters: microstructure and pore surface wettability. Carbon-fiber based porous materials, namely non-woven carbon paper and woven carbon cloth, have received wide acceptance as materials of choice for the PEFC GDL owing to their high porosity (~70% or higher) and good electrical/thermal conductivity. SEM micrographs of a carbon paper and a carbon cloth are shown in Fig. 1(a). Mathias *et al.*[11] provided a comprehensive overview of GDL structure and functions. In order to facilitate removal of liquid water from a GDL and avoid flooding, the GDL is treated with PTFE with loading varying from 5–30 wt% in order to induce and/or enhance hydrophobicity.[11] However, the wide range of wetting characteristics of carbon-based materials[8] as well as possible anomalies in the PTFE treatment might render some of the GDL pores hydrophilic. Furthermore, surface defects, impurities and ageing of the GDL might lead to a reduction in hydrophobicity, thereby causing mixed wettability surface characteristics. Recent experimental data of Gostick *et al.*[12] clearly showed the mixed wetting characteristics of the GDL. For efficient liquid water transport, the underlying pore morphology and wetting characteristics of the GDL must be carefully controlled and their roles well understood.

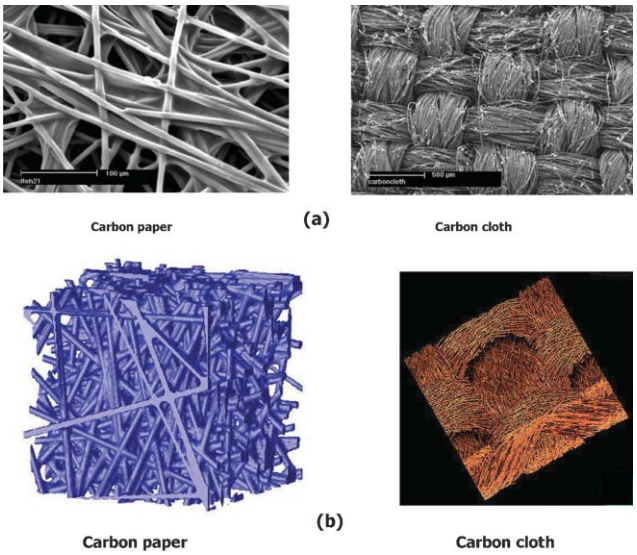

Fig. 1 SEM images and reconstructed digital microstructures[43] of carbon paper and carbon cloth GDLs.

Pore-scale modeling

A brief overview of popular pore-scale models is given here. Pore-scale models for solving flow, specifically two-phase flow and transport through porous media, can be broadly classified into rule-based and first-principle-based models. Rule-based models rely on incorporating adequate physics on top of an idealized network representation of the porous medium. Percolation models, diffusion-limited aggregation (DLA) models and anti-DLA models belong to this category. The most prominent among the rule-based models is the pore-network (PN) model. In PN modeling, the porous medium is represented by a network of wide pores connected by narrow regions called throats and the flow is solved on this network with the relevant physics taken into account.

PN modeling started with the pioneering work of Fatt[13–15] who computed capillary pressure and relative permeability in a network of interconnected pores. Since then, network models

Chao-Yang Wang

Chao-Yang Wang received his Ph.D. degree in Mechanical Engineering from the University of Iowa in 1994, and he is currently a Distinguished Professor of Mechanical Engineering and Professor of Materials Science and Engineering at the Pennsylvania State University. He has been the founding director of the Penn State Electrochemical Engine Center (ECEC) since 1997. His interests include transport and materials aspects of fuel cell and battery systems.

have become more sophisticated both in terms of reconstructing a physically realistic and topologically equivalent pore-network structure and incorporation of detailed flow dynamics in porous media.[16] Various researchers have predicted and experimentally validated capillary pressure and relative permeabilities for a range of soils and rocks with PN models and further investigated the effects of heterogeneity, mixed-wettability,[17,18] viscous ratio and injection rates[19] on relative permeability. In addition, the PN models have been applied to address a wide range of phenomena, such as transport in reactive porous media,[20] heat transfer[21] and drying in porous media.[22–25] While network models were initially developed to address flow in low-porosity and low-permeability porous media such as soils and rocks, Thompson[26] expanded their applicability to high-porosity and high-permeability fibrous media.

The first-principle-based approaches resolve the underlying transport processes by solving the governing partial differential equations (PDE). The PDEs can be solved by fine-scale computational fluid dynamics (CFD) methods. Alternatively, the molecular dynamics (MD), lattice gas (LG) and lattice Boltzmann (LB) methods can be employed.[27] With a given set of suitable boundary conditions, the PDEs can be properly discretized on a computational grid using standard CFD techniques, namely finite difference, finite volume or finite element methods. However, the lack of versatility of implementing the boundary conditions for arbitrary grain shapes makes the application of CFD-based two-phase models, such as multi-field, interface-tracking and volume-of-fluid approaches,[28] to a real porous medium exceedingly difficult. On the other hand, the MD approach[29–31] takes into account the movements and collisions of all individual molecules constituting the fluid with detailed description of the intermolecular interactions and thereby provides realistic equations of state characterizing the real fluid. However, the complexity of interactions, as well as the number of molecules representative of the actual fluid, make the molecular dynamics models computationally prohibitive for application to macroscopic flows in porous media.

The LB method and its predecessor LG method consider the behavior of a collection of particles comprised of large number of molecules moving on a regular lattice, thereby reducing the degrees of freedom of the system, and make the pore-scale simulation computationally tractable. Owing to its excellent numerical stability and constitutive versatility, the LB method has developed into a powerful technique for simulating fluid flows in recent years and is particularly successful in applications involving interfacial dynamics and complex geometries.[32–34] Wolf-Gladrow[27] and Succi[35] provided a formal description of the evolution of the LB method from its predecessor, the LG method.[36,37] LB methods consider flows to be composed of a collection of pseudo-particles residing on the nodes of an underlying lattice structure which interact according to a velocity distribution function. The LB method is an ideal scale-bridging numerical scheme which incorporates simplified kinetic models to capture microscopic or mesoscopic flow physics, and yet the macroscopic averaged quantities satisfy the desired macroscopic equations. As opposed to the front-tracking and front-capturing multiphase models in traditional CFD, the LB model, due to its kinetic nature, incorporates phase segregation and surface tension in multiphase flow through interparticle force/interactions, which are difficult to implement in traditional CFD methods.[38] While the LB modeling approach better represents the pore morphology in terms of a realistic digital realization of the actual porous medium and incorporates rigorous physical description of the flow processes as compared to the PN models, it is computationally more demanding.

Another type of pore-scale model is the full morphology (FM) model[39,40] based on morphological analysis of the digital representation of an actual porous medium. The FM model aims to link the macroscopic static properties, *e.g.* capillary pressure–saturation relation, to an accurate representation of the porous medium through direct input of the morphological information.

In this Feature Article, the PN, FM and LB models are discussed as mesoscopic simulation tools for the understanding of liquid water dynamics and associated constitutive relations in the GDL of a PEFC.

Microstructure generation

Construction of a realistic GDL pore morphology is an essential prerequisite to the pore-scale modeling. This can be achieved either by 3-D volume imaging or by constructing a digital microstructure based on stochastic models. Non-invasive techniques, such as X-ray and magnetic resonance micro-tomography, are the popular methods for 3-D imaging of pore structure. Another alternative is reconstruction of a microstructure using stochastic simulation techniques. The low cost and high speed of data generation make stochastic generation methods the preferred choice over the experimental imaging techniques.

As is evident from the SEM micrographs in Fig. 1(a), the non-woven carbon paper consists of well-defined carbon fibers with a fixed diameter and the fibers are randomly oriented leading to anisotropy in material properties along the through-plane and in-plane directions. On the other hand, the carbon cloth is comprised of fiber bundles laid out in a woven fashion with the basic element being a carbon fiber with fixed diameter. It is worth noting that in the carbon cloth, liquid water motion along individual fibers as well as between fiber bundles contributes to the overall flooding dynamics and hence is more involved as compared to the carbon paper. Based on a stochastic reconstruction technique, three-dimensional "digital" microstructures for carbon paper and carbon cloth, based on structural inputs, namely fiber diameter, fiber orientation, fiber-bundle dimension and porosity, have been created. Details about the reconstruction method as well as the underlying assumptions can be found in the works by Schladitz and co-workers.[41,42] Fig. 1(b) shows the generated digital structures of carbon paper and carbon cloth GDLs.[43] A comprehensive account of the structure generation of different commercial carbon paper GDLs and their structural characterization including pore size distribution and in-plane and through-plane permeability has been provided recently.[44] Fig. 2 shows a reconstructed SGL10BA® carbon paper GDL along with the structural parameters.[44]

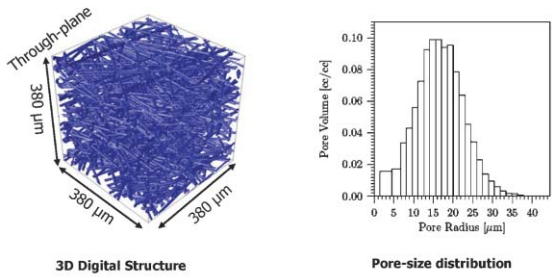

Permeability	In-plane	Through-plane	In-plane/Through-plane
Reconstructed GDL	30.9 darcy	21.1 darcy	1.46
Measured data	33 darcy	18 darcy	1.83

Fig. 2 Reconstructed SGL10BA® GDL and the corresponding structural parameters.[44]

3. Liquid water transport in a hydrophobic GDL

A fundamental understanding of liquid water transport in a hydrophobic GDL is first described. Two-phase flow in porous media is governed by capillary and viscous forces and their relative magnitude controls the two-phase distribution and flow regimes. Two-phase flow is designated as a drainage process if the invading fluid is non-wetting, and an imbibition process otherwise. Liquid water transport in a hydrophobic GDL is thus essentially a drainage process. Lenormand *et al.*[45] proposed a phase diagram, illustrated in Fig. 3, to describe displacement of a wetting phase by a non-wetting phase in the absence of buoyancy forces. They found that immiscible displacement is governed by capillary number, *Ca*, and viscosity ratio, *M*, defined as:

$$Ca = \frac{u\mu_{nw}}{\sigma} \qquad M = \frac{\mu_{nw}}{\mu_{wet}} \tag{1}$$

where subscripts 'nw' and 'wet' stand for the non-wetting and wetting phase respectively. u is the velocity of non-wetting phase and σ is the surface tension. Fig. 3 also shows characteristic distributions of the non-wetting phase in a two-dimensional cross section for all the three flow regimes.[45–47] For a typical fuel cell application, the viscosity ratio is 17.5 and capillary number is of the order of 10^{-8}; therefore, two-phase flow in a GDL falls in the regime of capillary fingering. For a detailed description of capillary fingering, readers may refer to ref. 46.

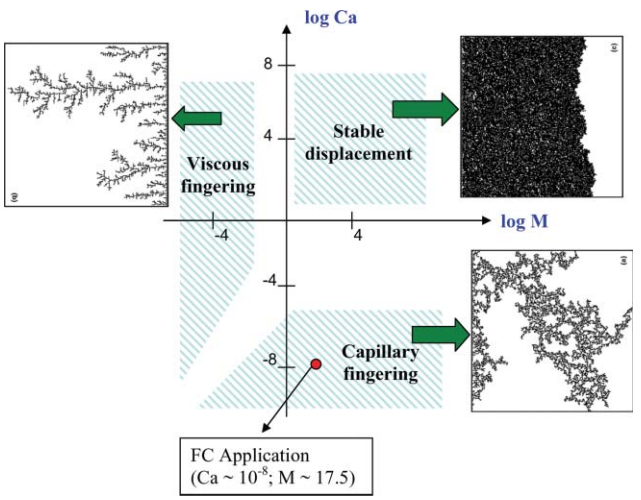

Fig. 3 Schematic representation of phase diagram showing various transport regimes and characteristic distribution of non-wetting phase for these regimes.[45–47]

Pore-network model

A physically realistic pore-network model of carbon paper GDL has been developed to elucidate liquid water transport in a GDL at the pore level, for the first time. Randomly distributed fibers in the carbon paper GDL result in highly disordered pore space topology; therefore, a high resolution three-dimensional image would be required to construct a topologically equivalent pore-network structure. As a first attempt, however, the methodology of Nam and Kaviany[6] is followed in which carbon paper is regarded to consist of randomly stacked regular fiber screens such that a three-dimensional random tetragonal pore-network structure with pores cubic in shape and throats of square cross-section is selected. In the present study, pore and throat radii are assumed to have a cut-off log normal distribution. Pore and throat radii are defined as the radii of the largest sphere that can be inscribed in a pore and a throat, respectively. In addition, a throat length is defined to characterize the throats in the network. For a throat connecting pores i and j, the throat length is given by:

$$l_{i,j} = L - (r_i + r_j) \tag{2}$$

where L is the distance between two adjacent pores and assumed to be constant in the present work.

The geometric and transport parameters used in the present PN model are summarized in Table 1. The absolute parameters of the present pore-network structure are summarized and compared with Toray® carbon paper parameters in Table 2. Recently, Gostick *et al.*[48] reported significant anisotropy in permeability for various carbon paper GDLs, with highly-aligned-fiber materials showing a maximum anisotropy factor of 2. Further research to incorporate permeability anisotropy in an equivalent pore-network structure for a carbon paper GDL is currently under way. Main assumptions made in the PN model are: 1) wetting properties are assumed to be constant in the network; 2) while the radius of a throat serves to define its hydraulic conductance, the volume contributed by the throats is assumed to be small relative to the pore volumes; 3) only one fluid can reside in a throat; 4) flow within a throat is assumed to be laminar and given by the Hagen–Poiseuille law; 5) the resistance offered by a pore to flow is assumed to be negligible; and 6) fluids are assumed to be incompressible.

In an invaded pore or throat the wetting phase (air for hydrophobic GDL) can always be present along the corners in the form of wetting films.[49] However, formation of wetting films along the corners is governed by the Concus and Finn[50] condition:

$$\theta + \gamma < 90^\circ \tag{3}$$

Table 1 Pore-network and transport parameters

Parameter	Value
Network Parameters	
Mean pore radius, r_{mean}	10 μm
Minimum pore radius, r_{min}	9 μm
Maximum pore radius, r_{max}	12.5 μm
Mean throat radius, rth_{mean}	6 μm
Minimum throat radius, rth_{min}	4 μm
Maximum throat radius, rth_{max}	8.5 μm
L	25 μm
Number of pores in x direction	11
Number of pores in y direction	30
Number of pores in z direction	30
Cut-off log-normal distribution: for pore and throat sizes	$f(r,\sigma_{nd}) = \frac{\sqrt{2}\exp\left[-0.5\left(\frac{\ln\left(r/r_{mean}\right)}{\sigma_{nd}}\right)^2\right]}{\sqrt{\pi\sigma_{nd}^2}r\left[erf\left(\frac{\ln\left(r_{max}/r_{mean}\right)}{\sqrt{2\sigma_{nd}^2}}\right) - f\left(\frac{\ln\left(r_{min}/r_{mean}\right)}{\sqrt{2\sigma_{nd}^2}}\right)\right]}$
Std. deviation in pore and throat size distribution, σ_{nd}	1.0
Transport Parameters	
Surface tension, σ	0.0625 N m^{-1}
Contact angle, θ	110° (for GDL with uniform wettability)
Dynamic viscosity of liquid water	3.5 × 10^{-4} Pa s
Dynamic viscosity of air	2.0 × 10^{-5} Pa s

Table 2 Comparison of pore-network structure parameters with Toray® carbon paper

Parameter	Pore-network model	Toray® carbon paper
Mean pore diameter	20 μm	16–25 μm[11]
Thickness	250 μm	110–370 μm[74]
Porosity	62%	78–80% (without PTFE loading and uncompressed)[74]
Absolute permeability (thickness direction)	5.6 Darcy[a]	5–10 Darcy[11]
Absolute permeability (in-plane direction)	6 Darcy	5–12 Darcy[11]
Anisotropy factor (in-plane/through-plane)	1.07	1.3 (uncompressed)[48]

[a] 1 Darcy = 10^{-12} m^2

where θ and γ are contact angles between wetting phase and solid matrix and half corner angle of a pore or a throat respectively. Thus, a contact angle between liquid water (non-wetting phase for hydrophobic GDL) and carbon fibers of 110° and square cross-section of pores and throats suppress the existence of wetting films along the corners. It should be mentioned that a small fraction of pores, having corner half angle less than 20°, in the actual pore spaces of carbon paper may allow simultaneous occupancy of a throat with both fluids. Incorporation of wetting film flow, in accordance with the Concus and Finn[50] condition, in a topologically equivalent pore-network structure of carbon paper is envisioned as a future extension of the present PN model.

For simplicity, the Hagen–Poiseuille law originally derived for circular tubes is used to represent the flow through a throat, although Patzek and Silin[51] analytically derived a generalized Poiseuille law to represent flow in a throat of square cross-section and showed the conductivity of a square throat is 20% lower. No substantial differences are expected as the pressure drop across a throat does not govern the transport at the small capillary numbers typically encountered in a PEFC operation. More details of the PN model and its numerical algorithms can be found in the work of Sinha and Wang.[52]

The liquid water transport in an initially dry GDL and in contact with a liquid reservoir is investigated with a constant injection rate boundary condition at the inlet face. The constant injection rate of liquid water is equivalent to 2.0 A cm^{-2} current density assuming that all the water produced is in liquid form. A constant pressure boundary condition is imposed on the outlet face with no coverage by liquid water assumed under high gas flow in the gas channel. A no-flow boundary condition is imposed on all the other faces.

Numerical visualization of liquid water front movement within the network during the drainage process is depicted in Fig. 4, where irregular fractal patterns typical of invasion percolation can be observed. It is clear from Fig. 4 that liquid water moves in the GDL through several continuous clusters. As liquid water invades into the GDL, the liquid water front encounters multiple dead ends. The pressure difference across a gas–liquid interface must be larger than the capillary pressure at the interface for liquid water to invade further. Dead ends to front propagation appear when a liquid water front reaches a very narrow region with a very large entry capillary pressure. When a liquid water front invades such a narrow region, the liquid water pressure increase at the inlet face makes the water fronts unstable at several locations and liquid water invades further into the GDL there. This mechanism can be more clearly explained with Fig. 5, where only ''open clusters'' during the liquid water transport in the GDL are displayed. The open clusters are defined as the liquid water clusters having non-zero flow rate at any instant of time.

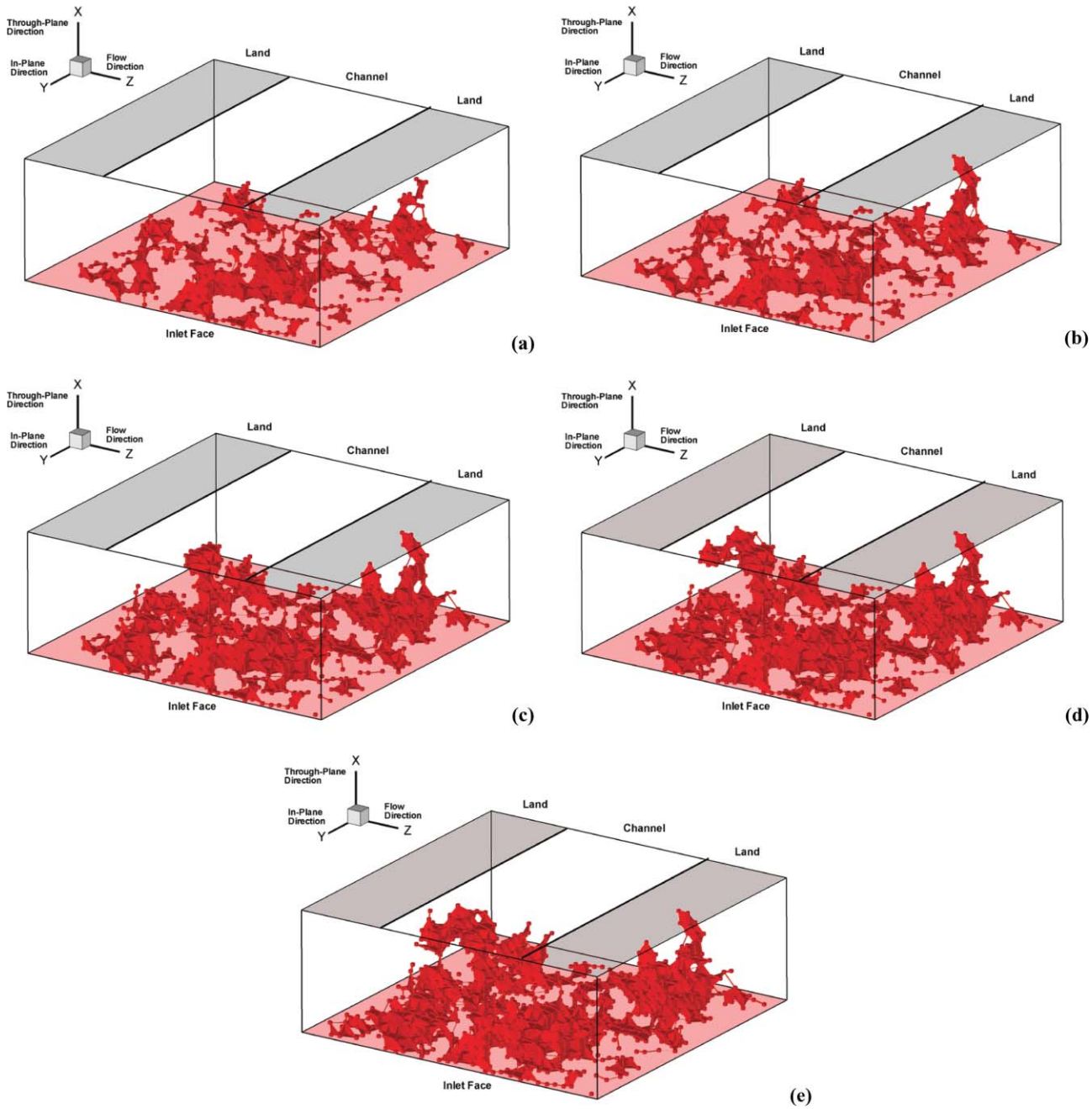

Fig. 4 Liquid waterfront movement in GDL: (a) to (d) at intermediate states, showing the evolution of capillary fingers, and (e) at steady state.

Fig. 5(a) shows the open clusters at an intermediate time step but as liquid water invades further into the GDL, these liquid water clusters encounter dead ends and liquid water starts flowing through other clusters in order to maintain constant flow rate at the inlet face, as shown in Fig. 5(b) and (c). As mentioned earlier, the capillary number for liquid water movement in a GDL under realistic operating conditions is $\sim 10^{-8}$. Thus, capillary forces control the transport of liquid water in GDL and liquid water follows a path of least resistance through the GDL.

Fig. 6(a) shows the evolution of the cross-sectional averaged liquid water saturation profile along the GDL thickness during water invasion. The saturation profiles shown in Fig. 6(a) are characteristic of fractal fingering flow. The occurrence of dead ends to multiple water clusters, originating from the inlet face, and the advancement of a single cluster following the path of least resistance, at low *Ca*, result in a convex shape of the steady-state saturation profile. In comparison, two-phase PEFC macroscopic models, published widely in the literature, invariably yield concave-shaped saturation profiles characteristic of stable displacement. Fig. 6(b) shows the steady-state liquid water saturation profiles for capillary number varying from 10^{-3} to 10^{-8} (by increasing the flow rate). As can be seen, the characteristics of the saturation profile change from a fractal form ($Ca = 10^{-8}$) to a stable flow form ($Ca = 10^{-4}$ and 10^{-3}) with increase in capillary number. This crossover from

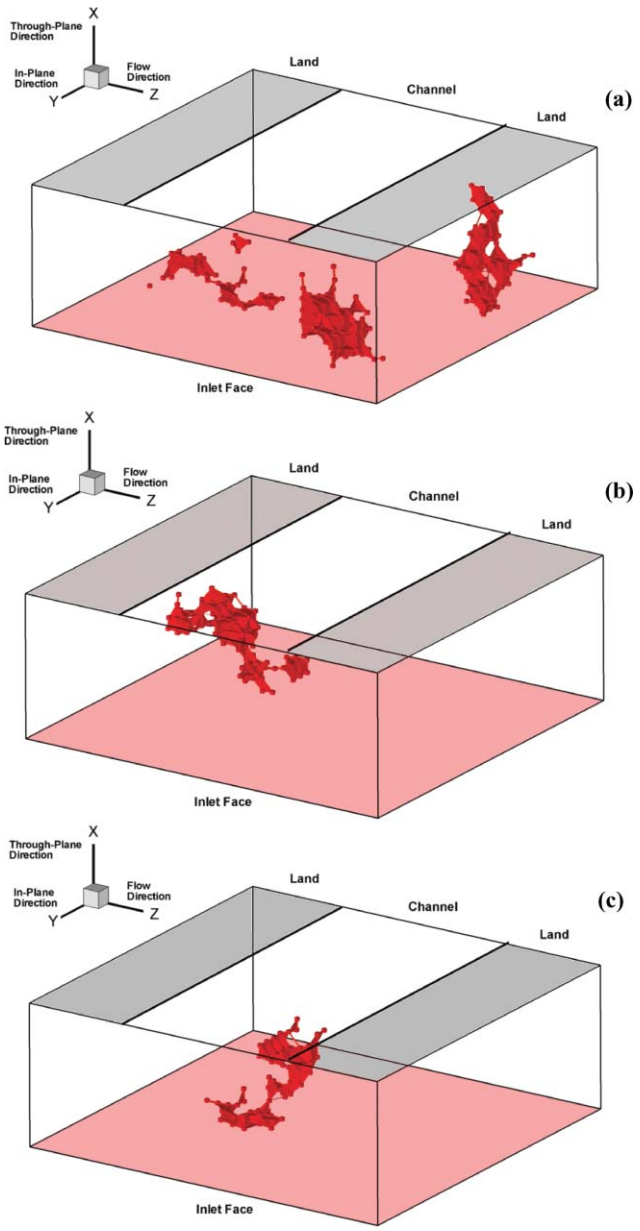

Fig. 5 Open liquid water clusters during liquid water transport in GDL at: (a) initial state, (b) intermediate state, and (c) steady state.

capillary fingering to stable front invasion during drainage has been experimentally observed and investigated in detail in other applications.[45,46,53,54] The crossover in the liquid flow regime shown in Fig. 6(b) also underpins the necessity to match the capillary number in any *ex-situ* experiments with that in an operating PEFC in order to properly characterize liquid water distribution in a GDL. This does not always happen in the literature; for instance, the *ex-situ* experiments by Djilali and co-workers[55,56] used a water injection rate equivalent to 112 A cm^{-2} current density.

Full morphology model

With a reconstructed GDL structure, the stationary distribution of air and water for a particular capillary pressure can be evaluated using the FM model *via* a simulated drainage

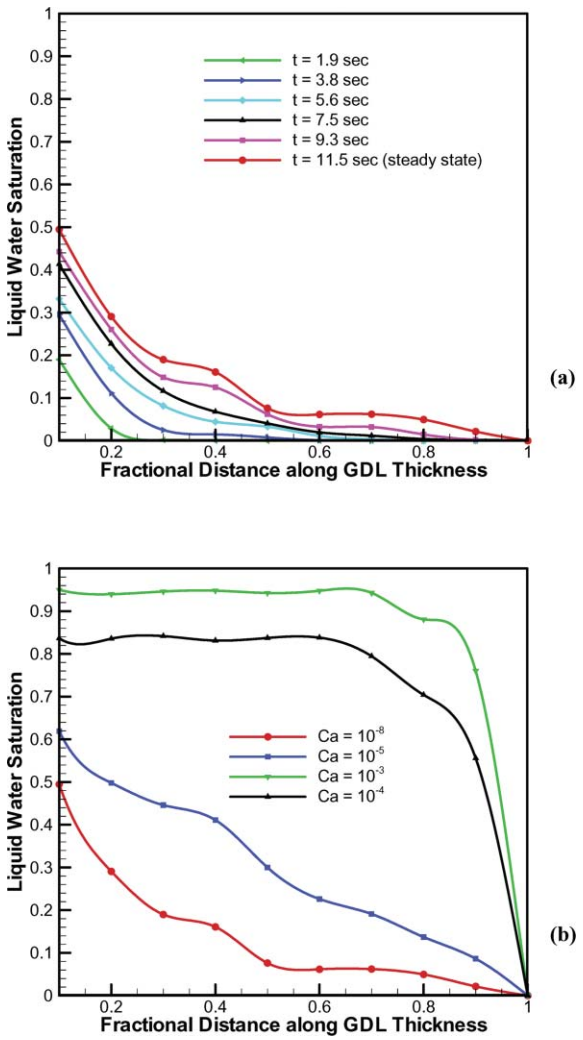

Fig. 6 (a) Evolution of liquid water saturation profiles along the GDL thickness, (b) steady state saturation profiles as a function of *Ca*.

process through an initially air-saturated GDL. The FM model relies on decomposing the 3-D digital image of the GDL with the pore radius as the ordering parameter at a specified pressure during drainage in order to determine the pore space to be accessible to the non-wetting phase (NWP).[40,44] The key steps in the simulated quasi-static drainage process with the FM model include:[44] 1) the entire pore space is filled with the wetting phase (WP) and the capillary pressure is zero. At one end, the porous medium is connected to a NWP reservoir while at the opposite end it is connected to the WP reservoir; 2) the pore space is eroded by a spherical structuring element with radius, r, corresponding to the capillary pressure, p_c, according to the Young–Laplace equation:

$$p_c = \frac{2\sigma\cos\theta}{r} \quad (4)$$

where σ is the surface tension between NWP and WP, and θ is the contact angle; 3) at a given capillary pressure, only those pores within the eroded pore space having a continuous connection to the NWP reservoir are filled with the NWP. The rest of the unconnected pores are removed from the eroded

space; 4) the phase saturations related to the capillary pressure are subsequently determined by dilating the eroded pore space and evaluating the corresponding occupied volume fractions of the pore space;[40,44] 5) the erosion–dilation process is repeated with the next larger spherical element corresponding to the capillary pressure.

Fig. 7 shows the liquid water distributions in a reconstructed SGL10BA® carbon paper GDL microstructure at various capillary pressure levels as predicted by the FM model.[44] At bubble point, the liquid water front reaches the air reservoir *via* a connected pathway through the GDL structure. From the liquid saturation map, it can be observed that with increasing capillary pressure, several liquid water fronts start penetrating into the air-saturated medium based on the pore size distribution and the resulting capillary force in the form of fractal fingering.

It is to be noted that the quasi-static two-phase distribution in the FM model is based on purely morphological consideration of overlapping spherical elements and therefore cannot accurately capture the effect of the interfacial shape on the invasion process.[44] A further implication of the spherical structural element assumption is that the current FM model is only applicable for diffusion media with uniform wettability. Incorporating the effect of interfacial shape based on the wetting characteristics is envisioned as a future extension to the current FM model. However, the FM model is a fast, direct simulation method based on actual pore morphology as opposed to network representation of the morphology in the PN model and the two-phase distributions obtained thereof can be useful in finding saturation-dependent effective transport properties, *e.g.* effective gas diffusivity, giving rise to a possibility for virtual design of novel GDL structures.[44,57] Detailed investigations with different reconstructed GDL pore morphologies are currently under way in order to discern the impact of underlying structure on the averaged phase distribution and therefore on the oxygen transport.

Lattice Boltzmann model

The LB model offers great promise to study the detailed liquid water dynamics through a realistic GDL structure. To this end, a two-phase LB model has been developed based on the interaction potential based model originally proposed by Shan and Chen[58–61] and henceforth will be referred to as the S–C model. In brief, the S–C model[58–61] introduces k distribution functions for a fluid mixture comprising of k components. Each distribution function represents a fluid component and satisfies the evolution equation. The non-local interaction between particles at neighboring lattice sites is included in the kinetics through a set of potentials. The evolution equation for the kth component can be written as:

$$f_i^k(\boldsymbol{x}+\boldsymbol{e}_i\delta_t,t+\delta_t)-f_i^k(\boldsymbol{x},t)=-\frac{f_i^k(\boldsymbol{x},t)-f_i^{k(\mathrm{eq})}(\boldsymbol{x},t)}{\tau_k} \qquad (5)$$

where $f_i^k(\boldsymbol{x},t)$ is the number density distribution function for the kth component in the ith velocity direction at position $\boldsymbol{x}$ and time t, and δ_t is the time increment. In the term on the right-hand side, τ_k is the relaxation time of the kth component in the lattice unit, and $f_i^{k(\mathrm{eq})}(\boldsymbol{x},t)$ is the corresponding equilibrium distribution function. The right-hand-side of eqn (5) represents the collision term based on the BGK (Bhatnagar–Gross–Krook), or the single-time relaxation, approximation.[62] Our LB model is designed for a three-dimensional 19-speed lattice (D3Q19, where D is the dimension and Q is the number of velocity directions).[60] The fluid/fluid interaction *via* the surface tension force and the fluid/solid interaction through the wall adhesion force are taken into account through the modified equilibrium distribution function corresponding to the interparticle interactions and hence the collision term. The macroscopic fluid phase properties are obtained through appropriate averaging of the particle distribution function.

In the present LB model for a GDL, equal density and viscosity values of the NWP and WP are assumed primarily

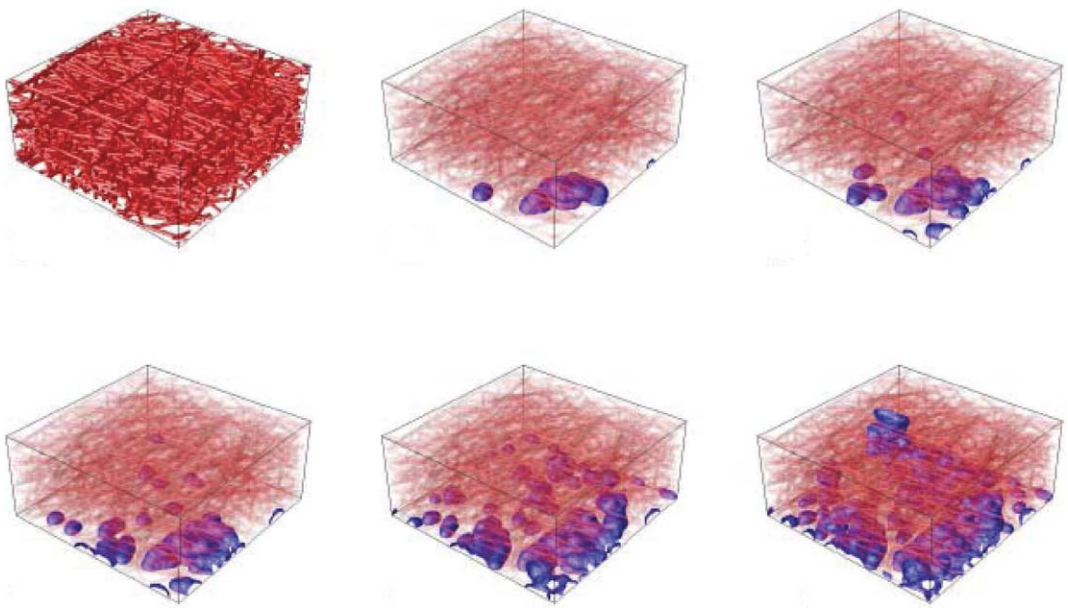

Fig. 7 Liquid water distribution in the reconstructed SGL10BA® GDL using the FM model.[44]

due to numerical instability arising from spurious currents at the phase interface, which is a feature of the S–C model. However, the assumption of negligible effects of the high density ratio ($\sim$1000) and viscosity ratio ($\sim$18) of air–water two-phase flow through a PEFC GDL could be very valid, because the system is characterized by very low values of *Ca* and *Re*, and consequently the surface forces indeed dominate over the inertial and viscous forces. Here *Re* is the Reynolds number defined as $Re = ud_p/v_{nw}$ with u the non-wetting phase velocity, d_p the characteristic pore diameter and v_{nw} the non-wetting phase kinematic viscosity. Additionally, the effect of gravitational force was shown to be negligible.[63]

A numerical experiment for a primary drainage (PD) simulation in a reconstructed carbon paper GDL with porosity of 72% and contact angle of 140° has been carried out using the afore-mentioned two-phase LB model.[64] The primary drainage process was simulated starting with zero capillary pressure, by fixing the NWP and WP reservoir pressures to be equal. Then the capillary pressure was increased incrementally by decreasing the WP reservoir pressure while maintaining the NWP reservoir pressure at the fixed initial value. The pressure gradient drives liquid water into the initially air-saturated GDL by displacing it. More details of the current LB model, the simulation set up, the model input parameters and the boundary conditions can be found in ref. 64 and 65.

Fig. 8 shows the liquid water distribution as well as the invasion pattern with increasing capillary pressure in the initially air-saturated carbon paper GDL. At the initial very low capillary pressure, the invading front overcomes the barrier pressure only at some preferential locations depending upon the pore size along with the emergence of a droplet owing to strong hydrophobicity. As the capillary pressure increases, several liquid water fronts start to penetrate into the air occupied domain. Further increase in capillary pressure exhibits growth of droplets at two invasion fronts, followed by the coalescence of the drops and collapsing into a single front. This newly formed front then invades into the less tortuous in-plane direction. Additionally, emergence of tiny droplets and subsequent growth can be observed in the constricted pores in the vicinity of the inlet region primarily due to strong wall adhesion forces from interactions with highly hydrophobic fibers with the increasing capillary pressure. One of the several invading fronts reaches the air reservoir at one location corresponding to the capillary pressure. The striking result from the LB simulation is the intricate liquid water dynamics through the fibrous structure and the droplet interactions with the highly hydrophobic fibers.

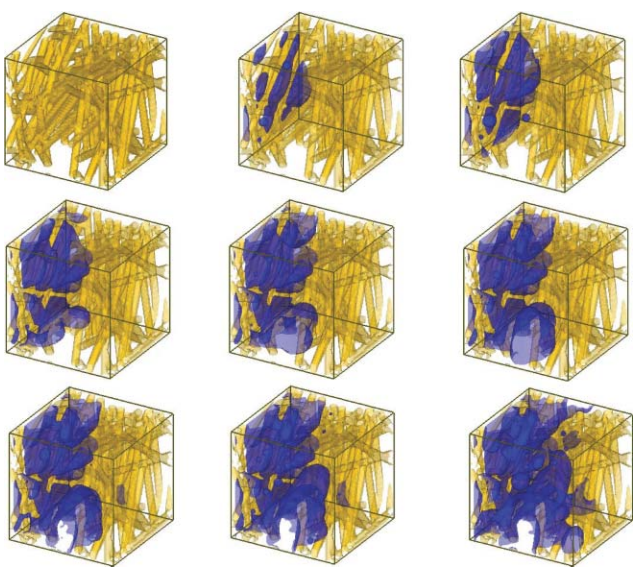

Fig. 8 Liquid water distribution in a reconstructed non-woven GDL microstructure from the drainage simulation using the two-phase LB model.

In order to better visualize the distribution of liquid water in GDL pores, contours of phase distributions corresponding to a representative liquid water saturation level at different cross-sections along the through-plane direction of the GDL are presented in Fig. 9. These 2-D saturation maps could aid in investigating the open area available for oxygen transport for a particular set of GDL morphological and wetting parameters and lead toward virtual design of next generation GDL structures for efficient water removal and reactant distribution.

Detailed investigations are currently under way regarding the drainage process with varying wettability through different GDL structures, along with numerical sensitivity study with respect to the sample size, boundary conditions, *etc*. A high density ratio and viscosity ratio LB model is also presently under development which will ultimately test the assumption of negligible effects of density and viscosity ratios in fuel cell applications. Finally, it is worth noting that a drainage simulation through a carbon cloth GDL is much more involved owing to liquid water motion along individual fibers as well as between fiber bundles. Developing a PN model for the carbon cloth is exceedingly difficult if not impossible, leaving the LB model perhaps the only choice for a detailed investigation of liquid water transport through the carbon cloth GDL.

4. Effect of wettability

Despite PTFE treatment, hydrophilic and hydrophobic pores co-exist in GDL materials. Few researchers[6,8,66] have

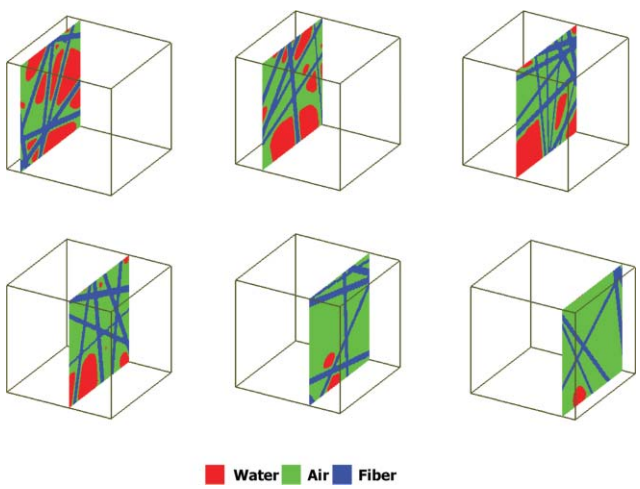

Fig. 9 2-D phase distribution maps on several cross-sections from the LB drainage simulation.

considered the GDL as partially hydrophilic. The most exhaustive treatment, to date, is perhaps given by Weber *et al.*,[8] who have taken mixed wettability of GDL into account *via* a composite contact angle as a function of the fraction of hydrophilic pores, *f*. They computed the maximum power and limiting current as functions of the fraction of hydrophilic pores, *f*, in GDL and showed the existence of an optimum value of *f* that entails a maximum value to limiting current and maximum power. However, the effect of mixed wettability on liquid water transport at the pore level was not examined in the prior literature. A fundamental understanding of the liquid water transport in a mixed-wet GDL is necessary to establish an optimal PTFE treatment protocol for GDLs.

Pore-network model

The PN model afore-described has been applied to study the effect of mixed wettability on liquid water transport in a GDL. The PN model is further modified to account for a contact angle distribution within the network. Since an accurate procedure to quantify the contact angle distribution inside the GDL is yet to be established, as a first approximation a uniformly random contact angle distribution is assumed, but correlated with the pore-throat sizes (*i.e.* larger throats are assigned larger contact angle). In the present work, contact angle is assumed to vary in the range of 100° to120° for the inlet and outlet throats, those connected to inlet and outlet faces respectively, and in the range of 65° to 120° in the inner layers of GDL. The rationale behind the assumption of contact angle higher than 90° for inlet and outlet throats is based on the non-zero capillary entry pressure in PTFE-treated GDL materials as experimentally found by Gostick *et al.*,[12] among others. Mixed-wettability of a GDL is quantified by *f*, the fraction of pore throats that are hydrophilic. Hence $f = 0$ represents a hydrophobic GDL in which contact angle is distributed in a range of 90° to 120°. The other pore-network parameters and the model assumptions remain the same. The following results are based on the average of eight realizations of contact angle distribution with the other structural parameters kept the same. For simplicity, no masking of the outlet face with land is implemented in the following calculations.

Liquid water transport in a mixed-wet GDL is comprised of local drainage and imbibition. For an interface to move, the following condition must be satisfied:

$$P_l - P_a > -P_c \quad \text{where} \quad P_c = \frac{2\sigma\cos\theta}{r} \tag{6}$$

where P_l, P_a and P_c denote the pressure of liquid water, air and capillary pressure respectively, r the pore or throat radius, σ the surface tension and θ the contact angle. For local drainage, eqn (6) shows that once a throat is filled, the adjacent pore will be automatically filled next. For local imbibition, pore filling is somewhat complex,[67] and follows a cooperative filling mechanism as elaborated by Valvatne and Blunt.[68] Also, wetting films cannot form along the corners,[50] and snap-off need not be considered.

The two-phase flow in a hydrophobic and a hydrophilic pore throat differs in that capillary pressure at the interface, P_c, resists liquid water transport in a hydrophobic pore throat while supporting it in a hydrophilic pore throat, as shown by eqn (6). This results in a preferential path for liquid water transport through the hydrophilic pore network in a mixed-wet GDL. Fig. 10 shows the steady-state liquid water distributions in different types of mixed-wet GDL for a typical realization of contact angle distribution. As shown in Fig. 10, the morphology of the liquid water front changes significantly with the hydrophilic fraction in a GDL. For GDL with $f = 0$, the liquid water distributions with constant contact angle of 110° and the distribution in the range of 90° to 120°, shown in Fig. 10(a) and (b), both feature fractal morphology. For a GDL with non-zero hydrophilic fraction, liquid water preferentially flows through the connected hydrophilic pore-network. As the hydrophilic fraction increases, the morphology changes from finger-like shape to piston-like compact shape, as shown in Fig. 10(c) and (d). The suppression of finger-shape morphology in a mixed-wet GDL can be explained by Fig. 11. Fig. 11(a) schematically illustrates that for a gas–liquid interface to move in a hydrophobic GDL, the pressure difference across the interface must exceed the capillary pressure of the connecting throat. Thus, for the invasion of liquid water in pore 2, liquid pressure in pore 2, P_l^2, must be higher than air pressure. Suppose the capillary pressure in the throat connecting pores 2 and 4 is low enough such that

$$P_l^2 - P_a^4 > P_c^{2,4} \tag{7}$$

where P_a^4 and $P_c^{2,4}$ denote the air pressure in pore 4 and the capillary pressure of the throat connecting pores 2 and 4, respectively. If eqn (7) is satisfied, the interface at the entrance of the throat connecting pores 2 and 4 grows unstable and liquid water will invade pore 4. However, if the throat connecting pores 2 and 3 is very narrow, as shown in Fig. 11(a), the interface cannot move from pore 2 into 3, incurring a dead end to liquid water flow. On the other hand, Fig. 11(b) depicts the liquid water movement in a mixed-wet GDL with the throat connecting pores 2 and 3 becoming hydrophilic while the rest of the parameters remain the same as in Fig. 11(a). In order for the liquid water interface to be stable at the entrance of the throat connecting pores 2 and 3, the following condition must be satisfied:

$$P_l^2 + |P_c^{2,3}| = P_a^3 \tag{8}$$

Again, when pore 2 is filled completely with liquid water, the liquid pressure in pore 2 is higher than air pressure as discussed earlier. This makes the interface unstable at the entrance of the throat connecting pores 2 and 3 irrespective of the connecting throat size. Thus, liquid water invades both the throats connecting pore 2 to pores 3 and 4 in the mixed-wet GDL, as shown in Fig. 11(b), which suppresses the occurrence of dead ends.

Fig. 11(c) shows the steady-state saturation profiles along the GDL thickness as a function of the hydrophilic fraction in a GDL averaged over eight realizations of contact angle distribution. As shown in Fig. 11(c), the shape of saturation profile changes from convex, typical of fractal fingering, to concave, typical of stable front, with increase in hydrophilic

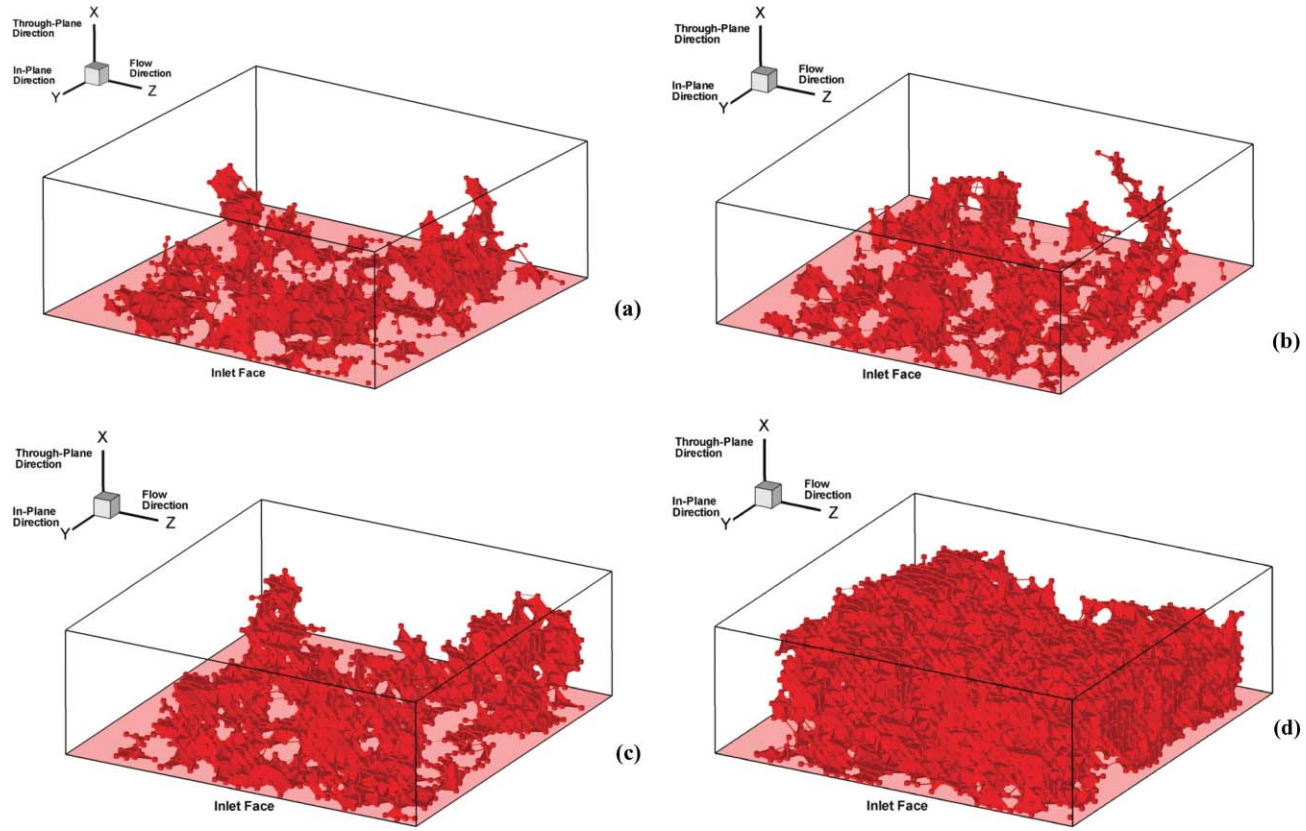

Fig. 10 Liquid water distribution in a (a) hydrophobic GDL with uniform contact angle of 110°, (b) hydrophobic GDL with contact angle distributed in a range of 90°–110°, (c) mixed-wet GDL with f = 10%, and (d) mixed-wet GDL with f = 20%. Results are shown for a typical realization of contact angle distribution.

fraction. However, the most significant effect of wettability distribution on liquid water transport is reflected by the saturation level at the inlet face. As shown in Fig. 11(c), the liquid saturation at the inlet face is smaller for a mixed-wet GDL with 10% hydrophilic fraction than that for a hydrophobic GDL. Physically, the inlet face corresponds to the GDL–CL interface. Thus, the lower the saturation at the inlet face, the lower the mass transport limitations due to GDL flooding. However, as the hydrophilic fraction in a mixed-wet GDL is further increased to 20%, the liquid saturation at the inlet face becomes higher, incurring significantly higher mass transport limitations to a PEFC operation. In addition, higher hydrophilic fraction increases the average liquid saturation in GDL, as shown in Fig. 11(c). This indicates the existence of an optimum hydrophilic fraction in a GDL that entails the least mass transport limitations.

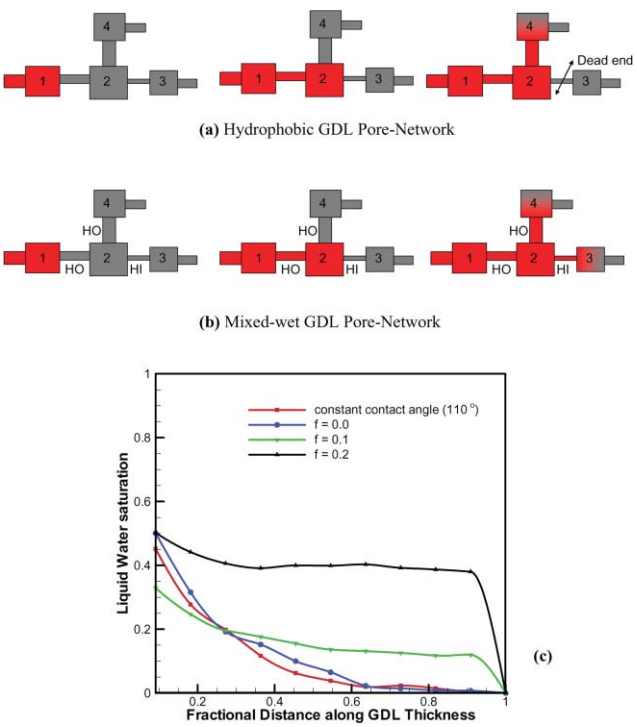

Fig. 11 Schematic representation of liquid water transport in: (a) a hydrophobic GDL, (b) a mixed-wet GDL, illustrating the suppression of dead ends in a mixed-wet GDL. (c) Liquid water saturation profiles as a function of the hydrophilic fraction f.

Lattice Boltzmann model

In order to discern the influence of wettability, the aforementioned two-phase LB model is applied to carry out a numerical experiment based on a steady-state flow experiment for porous media,[69] in which the two immiscible fluids are allowed to flow simultaneously until equilibrium is attained and the corresponding saturations, fluid flow rates and pressure gradients can be directly measured. The numerical experiment starts with an initial random distribution of the NWP and WP within the GDL microstructure such that the

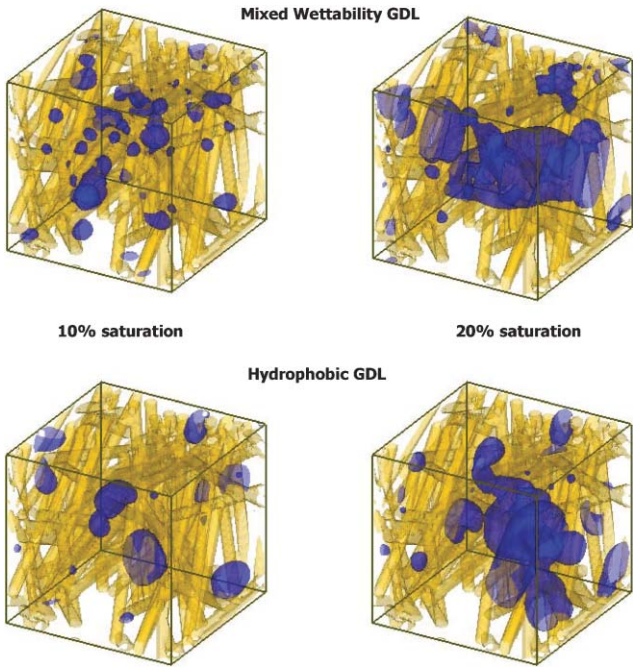

Fig. 12 Liquid water distribution for a hydrophobic and a mixed wettability GDL using the two-phase LB model.

desired NWP saturation is achieved. The GDL domain is bounded by walls in the span-wise directions and is periodic in the through-plane, *i.e.* the thickness, direction. Counter-current flow, characterized by opposing directions of transport of water and air, is simulated by adding a body force, in the S–C model for both phases, corresponding to the flow direction. The body force is adjusted such that the resulting capillary number is of the order 10^{-8}, representative of the GDL operation, as explained earlier. The details of the simulation set up, model input parameters and boundary conditions can be found in ref. 64 and 65.

Two wettability scenarios have been considered. Fig. 12 shows the equilibrium liquid water distribution with a purely hydrophobic GDL with contact angle of around 140° and a mixed wettability GDL with hydrophilic and hydrophobic contact angles of 80° and 140° respectively. In the mixed wettability GDL, a hydrophilic pore fraction of 50% is considered and the hydrophilic pores are assumed to be randomly distributed through the GDL structure. It can be observed that at the same saturation level, the liquid water distribution is quite different for the two GDLs, underscoring the influence of the wetting characteristics on transport processes. Additionally, Fig. 13 exhibits the 2-D phase distributions on several cross-sections for 20% saturation level. The liquid water saturation distributions from such a study could be further used to quantify the averaged saturation-dependent effective transport properties (*e.g.* effective species diffusivity) and the knowledge obtained from the simulations could be deployed in designing better GDL structures for efficient water removal.

5. Interfacial dynamics of water

Aside from the liquid water motion through a GDL, the interfacial behavior and dynamics of water, at both GDL–CL and GDL–channel interfaces, are of paramount importance. The LB model described above is also applicable to delineate water behaviors at these interfaces. In addition, micron-resolution visualization techniques have been developed to characterize these interfacial phenomena. Wang and co-workers[63,70] described a technique of combining a transparent fuel cell with a video microscope to visualize water droplet dynamics on the GDL–channel interface in an operating fuel cell under automotive operating conditions. Fig. 14(a) displays typical water droplets of a few hundred microns in size that emerge on the GDL surface, and Fig. 14(b) compares the measured and predicted droplet detachment diameter as a function of the air velocity in the gas channel. The theoretical

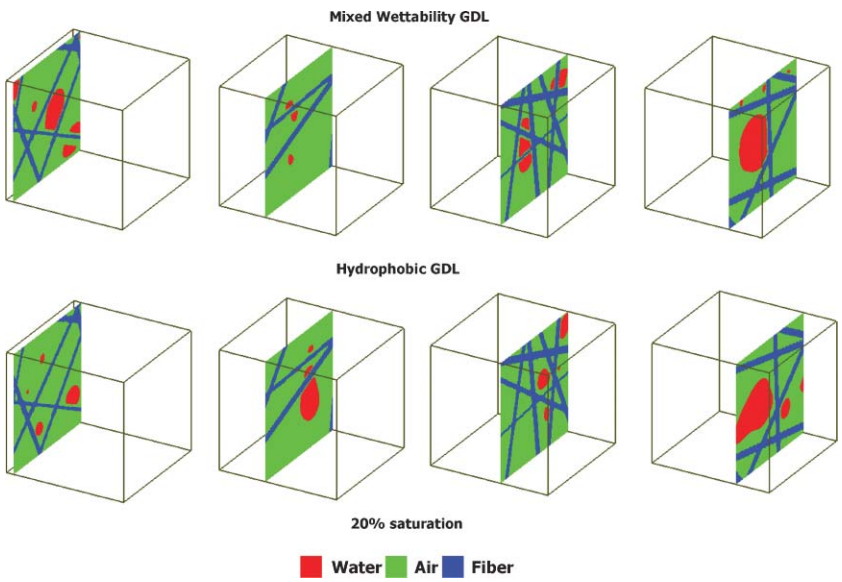

Fig. 13 2-D phase distribution maps on several cross-sections for a hydrophobic and a mixed wettability GDL from the two-phase LB model.

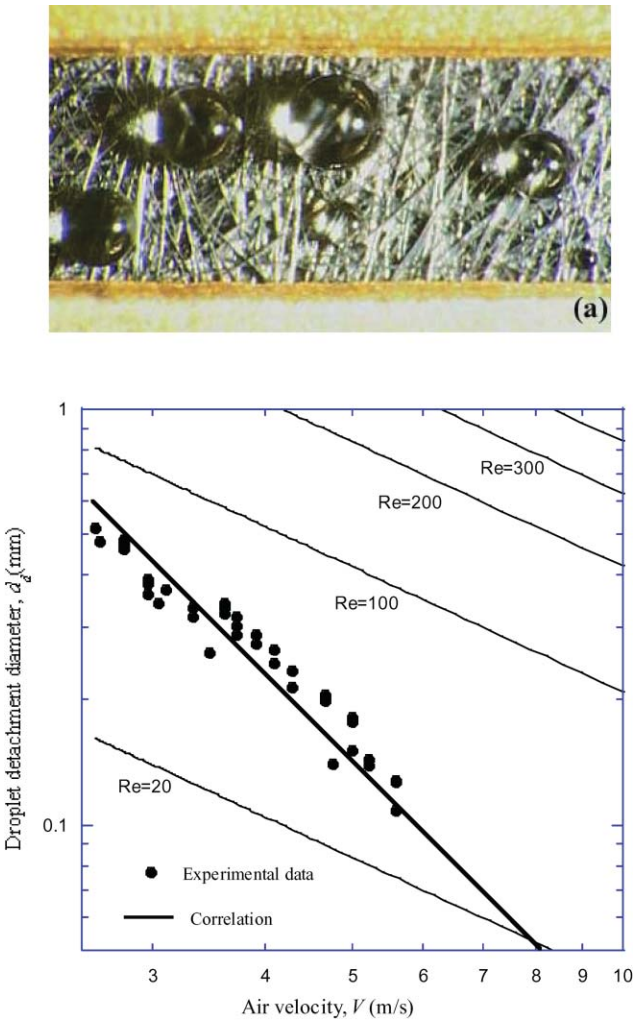

Fig. 14 (a) Water droplets grown on the GDL surface in a gas channel of 1 mm wide, and (b) the droplet detachment diameter as a function of air velocity in the channel.[70]

prediction was based on a simple model by balancing shear stress on a drop with the adhesion force on the GDL surface.[70]

The water dynamics on the CL surface in an operating fuel cell may also be visualized, albeit with higher spatial resolution. Most recently, Ge and Wang[71] disclosed a simple technique using regular GDL punched with microholes to create optical access to the CL surface. Fig 15 displays a typical image of water droplets on the CL surface. Such visualization studies coupled with pore-level modeling promise to unlock the mystery of water dynamics at various interfaces in a fuel cell. In particular, research is under way to visualize and identify interfacial dynamics of water in the temperature range of 5–80 °C, representative of a whole spectrum from PEFC startup to full operation.

6. *In-situ* pore-level characterization

Due to the inadequacy of the current visualization techniques in spatial resolution it is imperative to develop *in-situ* imaging techniques for both microscale pore geometry and liquid water distribution in the GDL of an operational fuel cell. In this

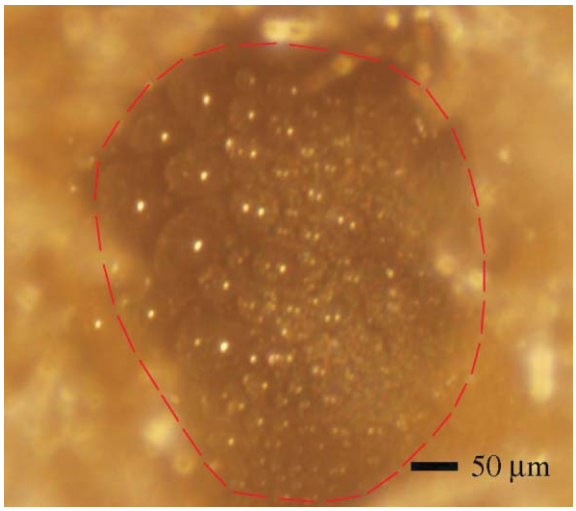

Fig. 15 Imaging of liquid water dynamics on the catalyst layer surface in an operating fuel cell with micron resolution.[71]

regard it is worth mentioning a new technique most recently proposed to quantitatively image liquid water distribution in a GDL by using X-ray or synchrotron-based X-ray micro-tomography. As a first step, Sinha *et al.*[72,73] successfully measured the liquid water saturation distributions in the cathode GDL during gas purge as well as fuel cell operation, achieving a spatial resolution of ~10 μm. Fig. 16 displays the experimental set up consisting of an X-ray CT imaging system, the OMNI-X HD600, a PEFC with 1 cm^2 active area, fuel inlet and outlet lines and thermal heating system. The PEFC is operated at different current densities with operating temperature and pressure of 50 °C and 1 atm, respectively, and with anode and cathode stoichiometry of 4. The cell fixture is rotated 360° in the X-ray beam while the two-dimensional array of detectors provides the attenuated views to the data acquisition computer. The GDL is scanned in 17 slices along the thickness, with the voxel dimension of 10 × 10 × 12 microns. Liquid water can be readily visualized along the GDL thickness as shown in Fig. 17, where the liquid water distributions are shown at different locations along the flow direction facing channel and land regions, respectively. The amount of liquid water is indicated by the color bar shown in Fig. 17. Substantial development and refinement of X-ray micro-tomography currently under way for the application to fuel cells offers an enhancement in the spatial resolution to ~1 μm, as desired to quantify liquid water distribution in GDL at the pore level as well as in the CL and microporous layer.

7. Summary

Automotive, stationary and portable applications stimulate an ever-increasing demand for the development of advanced fuel cell technologies with high performance, low cost, and extended durability. In the past decade, substantial experimental and modeling research has yielded a macroscopic understanding of intricate physicochemical processes in a PEFC. Nevertheless, much remains to be learned about the basics of liquid water transport and ensuing flooding in a GDL. An expansion of the present research perspective to

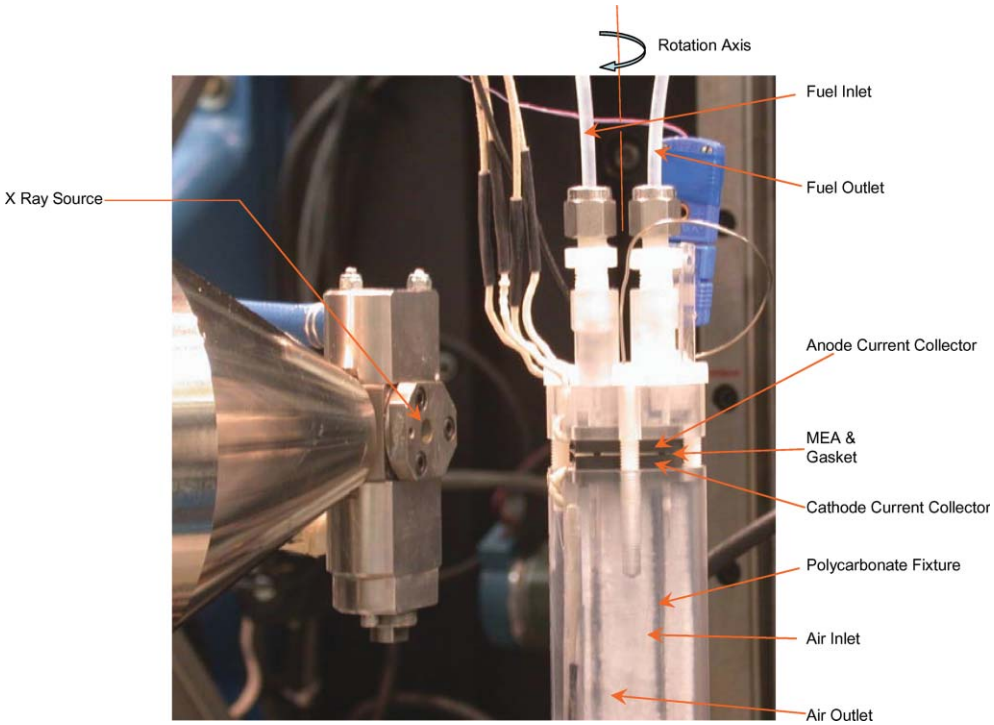

Fig. 16 X-Ray micro-tomography experimental setup to quantify liquid water distribution in anode and cathode GDL of an operating PEFC.[73]

address the roles of microstructural and surface wetting properties of key components such as GDL and CL is urgently needed in order to paint a clear picture of how flooding occurs and to determine the controlling factors. This can be best achieved through a combination of pore-scale modeling and micron-resolution characterization techniques, as briefly reviewed in the present Feature Article.

Finally, in addition to the enhancements of the current pore-scale modeling as well as imaging techniques as suggested earlier, it is imperative to develop experimental methods to quantitatively characterize the wettability of GDL pore walls which will allow further insight into the structure-wettability dependence of water management in PEFCs.

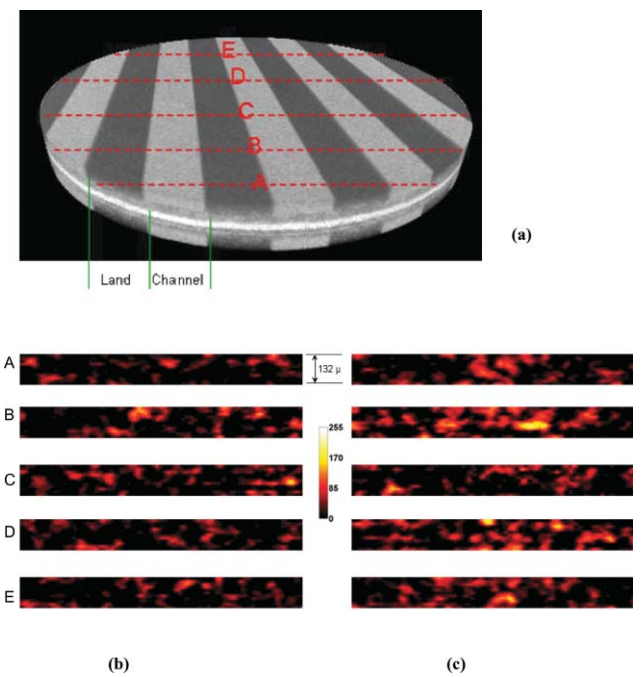

Fig. 17 (a) Three-dimensional X-ray CT image of anode and cathode porous layers and membrane assembly in a PEFC, scanned in dry state; visualization of liquid water distribution in cathode GDL facing (b) channel and (c) land region for a PEFC operating at 0.5 A cm^{-2} current density. The amount of liquid water is indicated by the color bar shown in the middle.[73]

Acknowledgements

We would like to thank Drs V. P. Schulz, A. Wiegmann and J. Becker from Fraunhofer ITWM, Germany for collaboration with GDL structure generation and FM modeling, Professor Philip Halleck of Penn State for collaboration on X-ray micro-tomography, and Dr Richard Steinberger of ECEC for his contributions to X-ray micro-tomographic results.

References

1 C. Y. Wang, in *Handbook of Fuel Cells – Fundamentals, Technology and Applications*, ed. W. Lietsich, A. Lamm and H. A. Gasteiger, John Wiley & Sons, Chichester, 2003, vol. 3, ch. 29, p. 337.
2 C. Y. Wang, *Chem. Rev.*, 2004, **104**, 4727.
3 A. Faghri and Z. Guo, *Int. J. Heat Mass Transfer*, 2005, **48**, 19.
4 W. J. S. He and T. V. Nguyen, *AIChE J.*, 2000, **46**, 2053.
5 Z. H. Wang, C. Y. Wang and K. S. Chen, *J. Power Sources*, 2001, **94**, 40.
6 J. H. Nam and M. Kaviany, *Int. J. Heat Mass Transfer*, 2003, **46**, 4595.
7 U. Pasaogullari and C. Y. Wang, *J. Electrochem. Soc.*, 2004, **151**, 399.
8 A. Z. Weber, R. M. Darling and J. Newman, *J. Electrochem. Soc.*, 2004, **151**, 1715.

9 Y. Wang and C. Y. Wang, *J. Electrochem. Soc.*, 2006, **153**, 1193.
10 H. Ju, G. Luo and C. Y. Wang, *J. Electrochem. Soc.*, 2007, **154**, 218.
11 M. F. Mathias, J. Roth, J. Fleming and W. Lehnert, in *Handbook of Fuel Cells – Fundamentals, Technology and Applications*, ed. W. Lietsich, A. Lamm and H. A. Gasteiger, John Wiley & Sons, Chicester, 2003, vol. 3, ch. 42, p. 517.
12 J. T. Gostick, M. W. Fowler, M. A. Ioannidis, M. D. Pritzer, Y. M. Volfkovich and A. Sakars, *J. Power Sources*, 2006, **156**, 375.
13 I. Fatt, *Trans. Am. Inst. Min. Metall. Eng.*, 1956, **207**, 144.
14 I. Fatt, *Trans. Am. Inst. Min. Metall. Eng.*, 1956, **207**, 160.
15 I. Fatt, *Trans. Am. Inst. Min. Metall. Eng.*, 1956, **207**, 164.
16 M. J. Blunt, M. D. Jackson, M. Piri and P. H. Valvatne, *Adv. Water Resour.*, 2002, **25**, 1069.
17 M. J. Blunt, *SPE J.*, 1997, **2**, 70.
18 A. Al-Futaisi and T. W. Patzek, *J. Contam. Hydrol.*, 2004, **74**, 61.
19 M. J. Blunt and P. King, *Transp. Porous Media*, 1991, **6**, 407.
20 J. S. Andrae, Jr., D. A. Street, Y. Shibusa, S. Havlin and H. E. Stanley, *Phys. Rev. E*, 1997, **55**, 772.
21 X. Li and Y. C. Yortsos, *AIChE J.*, 1995, **41**, 214.
22 J. B. Laurindo and M. Prat, *Chem. Eng. Sci.*, 1996, **51**, 5171.
23 Y. L. Bray and M. Prat, *Int. J. Heat Mass Transfer*, 1999, **42**, 4207.
24 A. G. Yortsos, A. K. Stubos, A. G. Boudouvis and Y. C. Yortsos, *Adv. Water Resour.*, 2001, **24**, 439.
25 A. G. Yortsos, A. G. Boudouvis, A. K. Stubos, I. N. Tsimpanogiannis and Y. C. Yortsos, *Phys. Rev. E*, 2003, **68**, 037303.
26 K. E. Thompson, *AIChE J.*, 2002, **48**, 1369.
27 D. A. Wolf-Gladrow, *Lattice gas cellular automata and lattice Boltzmann models: an introduction*, Springer-Verlag, Heidelberg, 2000.
28 G. F. Hewitt, S. Banerjee, S. Zaleski and G. Tryggvason, presented at *Short Courses: Modeling and Computation of Multiphase Flows, Part II B*, Zurich, Switzerland, 2001.
29 D. J. Evans and G. P. Morris, *Phys. Rev. E*, 1983, **51**, 1776.
30 G. A. Bird, *Molecular Gas Dynamics and the Direct Simulation of Gas Flows*, Clarendon, Oxford, 1994.
31 D. C. Rapaport, *The Art of Molecular Dynamics Simulation*, Cambridge University Press, 1995.
32 S. Chen and G. Doolen, *Ann. Rev. Fluid Mech.*, 1998, **30**, 329.
33 L.-S. Luo, *Proceedings of the International Conference on Applied Computational Fluid Dynamics*, ed. J.-H. Wu and Z.-H. Zhu, Beijing, China, 2000, p. 52–83 .
34 D. Raabe, *Model. Simul. Mater. Sci. Eng.*, 2004, **12**, R13.
35 S. Succi, *The Lattice Boltzmann Equation for Fluid Dynamics and Beyond*, Oxford University Press, Oxford, 2001.
36 D. H. Rothman and S. Zaleski, *Lattice Gas Cellular Automata*, Cambridge University Press, Cambridge, 1997.
37 J. P. Rivet and J. P. Boom, *Lattice Gas Hydrodynamics*, Cambridge University Press, Cambridge, 2001.
38 C. Pan, Ph. D. Dissertation, Univ. of North Carolina, Chapel Hill, North Carolina, 2003.
39 R. D. Hazlet, *Transp. Porous Media*, 1995, **20**, 21.
40 M. Hilpert and C. T. Miller, *Adv. Water Resour.*, 2001, **24**, 243.
41 K. Schladitz, S. Peters, D. Reinel-Bitzer, A. Wiegmann and J. Ohser, Technical Report 72, Fraunhofer ITWM, Germany, 2005.
42 K. Schladitz, S. Peters, D. Reinel-Bitzer, A. Wiegmann and J. Ohser, *Comput. Mater. Sci.*, 2006, **38**, 56.
43 Personal communications with Dr A. Wiegmann and Dr V. P. Schulz, Fraunhofer ITWM, Germany.
44 V. P. Schulz, J. Becker, A. Wiegmann, P. P. Mukherjee and C. Y. Wang, *J. Electrochem. Soc.*, 2007, **154**, B419.
45 R. Lenormand, E. Touboul and C. Zarcone, *J. Fluid Mech.*, 1998, **189**, 165.
46 R. Lenormand, *J. Phys.: Condens. Matter*, 1990, **2**, SA 79.
47 R. P. Ewing and B. Berkowitz, *Adv. Water Resour.*, 2001, **24**, 309.
48 J. T. Gostick, M. W. Fowler, M. D. Pritzker, M. A. Ioannidis and L. M. Behra, *J. Power Sources*, 2006, **162**, 228.
49 M. A. Ioannidis and I. Chatzis, *Chem. Eng. Sci.*, 1993, **48**, 951.
50 P. Concus and R. Finn, *Appl. Math. Sci.*, 1969, **63**, 292.
51 T. W. Patzek and D. B. Silin, *J. Colloid Interface Sci.*, 2001, **236**, 295.
52 P. K. Sinha and C. Y. Wang, *Electrochim. Acta*, submitted.
53 M. Ferer, G. S. Bromhal and D. H. Smith, *Physica A*, 2003, **319**, 11.
54 M. Ferer, G. S. Bromhal and D. H. Smith, *Phys. Rev. E*, 2003, **67**, 051601.
55 S. Litster, D. Sinton and N. Djilali, *J. Power Sources*, 2006, **154**, 95.
56 A. Bazylak, D. Sinton, Z. S. Liu and N. Djilali, *J. Power Sources*, 2007, **163**, 784.
57 V. P. Schulz, P. P. Mukherjee, J. Becker, A. Wiegmann and C. Y. Wang, presented at Electrochemical Society Meeting, Cancun, Mexico, October 29–November 3, 2006.
58 X. Shan and H. Chen, *Phys. Rev. E*, 1993, **47**, 1815.
59 X. Shan and H. Chen, *Phys. Rev. E*, 1994, **49**, 2941.
60 X. Shan and G. D. Doolen, *J. Stat. Phys.*, 1995, **81**, 379.
61 X. Shan and G. D. Doolen, *Phys. Rev. E*, 1996, **54**, 3614.
62 P. Bhatnagar, E. Gross and M. Krook, *Phys. Rev.*, 1954, **94**, 511.
63 X. G. Yang, F. Y. Zhang, A. Lubawy and C. Y. Wang, *Electrochem. Solid-State Lett.*, 2004, **7**, A408.
64 P. P. Mukherjee and C. Y. Wang, to be submitted.
65 P. P. Mukherjee and C. Y. Wang, presented at Electrochemical Society Meeting, Cancun, Mexico, October 29–November 3, 2006.
66 L. Pisani, G. Murgia, M. Valentini and B. D' Aguanno, *J. Electrochem. Soc.*, 2002, **149**, A898.
67 R. Lenormand and C. Zarcone, *SPE J.*, 1984, 13264.
68 P. H. Valvatne and M. J. Blunt, *Water Resour. Res.*, 2004, **40**, W07406.
69 D. Tiab and E. Donaldson, *Petrophysics: Theory and Practice of Measuring Reservoir Rock and Transport Properties*, Gulf Publishing Company, Houston, 1996.
70 F. Y. Zhang, X. G. Yang and C. Y. Wang, *J. Electrochem. Soc.*, 2006, **153**, A225.
71 S. Ge and C. Y. Wang, *Electrochim. Acta*, 2007, **52**, 3965.
72 P. K. Sinha, P. Halleck and C. Y. Wang, *Electrochem. Solid-State Lett.*, 2006, **9**, A344.
73 P. K. Sinha, R. Steinberger, P. Halleck and C. Y. Wang, ECEC Technical Report 2006-03, The Pennsylvania State University, University Park, PA, 2006.
74 Toray Industries Inc., http://www.toray.com/.